The zonal equatorial wind switch of IOD variability: Lessons from a simple reduced-gravity modelling study

J. Kämpf[1]

[1]College of Science and Engineering, Flinders University, Adelaide, Australia

Corresponding author: Jochen Kämpf (jochen.kaempf@flinders.edu.au)

Key Points:

- Uses a reduced-gravity model to study the ocean's response to wind forcing in the southeast tropical Indian Ocean
- Shows that equatorial wind is an exclusive control of the development of positive phases of the Indian Ocean Dipole
- Explains this by a Kelvin-wave response to equatorial perturbations of the thermocline

Abstract

Using a reduced-gravity model, this study explores the ocean's response to wind forcing in the South-East Tropical Indian Ocean (SETIO) during the development phase (July-September) of positive phases of the Indian Ocean Dipole (IOD), using the years of 2009 and 2019 for comparison. Findings show that IOD variability is exclusively controlled by zonal equatorial wind anomalies. In the average situation, represented by the 2009 season, westerly equatorial winds create downwelling Kelvin waves that operate to suppress the Sumatran upwelling. In contrast, positive phases of the IOD, represented by the 2019 season, are characterized by easterly equatorial winds that reverse the equatorial influence, which leads to strong coastal upwelling off Sumatra's southeast coast. In addition, findings show that the Sumatran upwelling involves the formation of a strong northwestward surface flow, the South-East Sumatra Current, that transports colder seawater into the region, which contributes to the IOD anomaly.

Plain Language Summary

The Indian Ocean Dipole (IOD) is a mode of natural year-to-year climate variability that strongly influences rainfall extremes in countries bordering the Indian Ocean. The positive phase of the IOD is characterized by the cooling of surface waters off Sumatra's southwest coast. This study uses a simplified computer model to explore the ocean's response to wind forcing characterizing different phases of the IOD. Findings reveal that the ocean's response exclusively depends on the direction of equatorial wind in the eastern Indian Ocean. The wind direction determines whether the surface layer of the ocean shoals or deepens along the equator, leading to a Kelvin wave disturbance that either enhances or suppresses the appearance of cold surface water off Sumatra's southwest coal. Concludingly, the direction of equatorial wind appears as a principal driver of IOD variability.

1 Introduction

The Indian Ocean Dipole (IOD) is a coupled atmosphere-ocean mode of interdecadal climate variability that strongly affects rainfall variability and extremes in countries bordering the Indian ocean (e.g., Saji and Yamagata, 2003; Behera et al., 2005; Chan et al., 2008; Cai et al., 2009; Qiu et al., 2014). Improved forecasting of IOD variability and how this variability will change under the global warming scenario has a high research priority in the climate sciences.

The IOD, first described by Saji et al. (1999), is a pattern of sea surface temperature (SST) fluctuations between the eastern and western intertropical Indian Ocean that can be characterized by the difference in SSTs of defined areas, called the Dipole Mode Index (DMI). Positive phases of the IOD, called pIOD events, are dominated by the widespread cooling of the surface ocean off Sumatra's southwest coast. SST anomalies tend to peak in late austral winter and spring (August to November) (Kämpf and Kavi, 2019). pIOD events are traditionally defined by DMI values exceeding 1°C for a period exceeding 12 weeks. After this definition, only four significant cooling events occurred in the years 1994, 1997, 2006 and 2019 since 1988 (see Kämpf and Kavi 2019). Hence, the occurrence of pronounced pIOD events is relatively rare.

The development of pIOD events is often explained by the Bjerknes feedback (Bjerknes, 1966, 1969), wherein an initial cooling off the coast of Sumatra–Java suppresses local atmospheric convection, leading to anomalous easterly wind, a shoaling thermocline and stronger upwelling which in turn reinforce the initial cooling (Saji et al. 1999; Webster et al. 1999; Feng and Meyers 2003; Cai et al. 2014, 2018). Lu and Ren (2020) suggested that a record-breaking interhemispheric sea-level pressure gradient between Australia and the South China Sea/Philippine Sea forming from May 2019 induced anomalously strong southeasterlies along Sumatra's coast as a cause of the subsequent pIOD event through the Bjerknes feedback.

Kämpf and Kavi (2019) presented an analytical theory of wind-driven upwelling along a coastline of finite length based on Kelvin-wave propagation. This theory suggests that wind-driven coastal Kelvin waves initiated near the equator can strongly modify the Sumatran upwelling. Analytical results derived from this theory were consistent with the statistics of pIOD events. It should be noted that the theory did not account for the effects of zonal equatorial wind anomalies. Kämpf and Kavi (2019) also analyzed the surface dynamic height field characteristic of pIOD events. This analysis infers the formation of a northwestward geostrophic surface flow, called the South-West Sumatra Current (SWSC), that has the potential to transport colder water into the region.

Kavi and Kämpf (2022) reported the existence of short-lived atmospheric cyclones in the South-Eastern Tropical Indian Ocean (SETIO), referred to as SETIO cyclones, comprising westerly equatorial wind bursts and northwesterly wind anomalies along Sumatra's coast. Findings indicate that SETIO cyclones operate to weaken the Sumatran upwelling, and that pIOD events follow from the relative absence of SETIO cyclones that intensifies southeasterlies along Sumatra's coast. Interestingly, the formation of SETIO cyclones commences with westerly equatorial wind bursts, which is like the Pacific situation, where such wind bursts lead to the suppressing of the Peru upwelling in El-Niño events (e.g., McPhaden 1999). It should be highlighted that SETIO cyclones already start to form in early austral winter from July, which precedes the timing of SST anomalies of pIOD events by 1-2 months (see Kavi and Kämpf, 2022).

Equatorial zonal wind induces coastal upwelling or downwelling off Sumatra's west coast through the so-called lee effect (Hela 1976, Kämpf 2015). Equatorial wind also induces upwelling or downwelling through the horizontal flow divergence it creates. The resulting thermocline disturbances can only propagate eastward along the equator in the form of an equatorial Kelvin Wave and southeastward along Sumatra's coast as a coastal Kelvin wave (**Figure 1**).

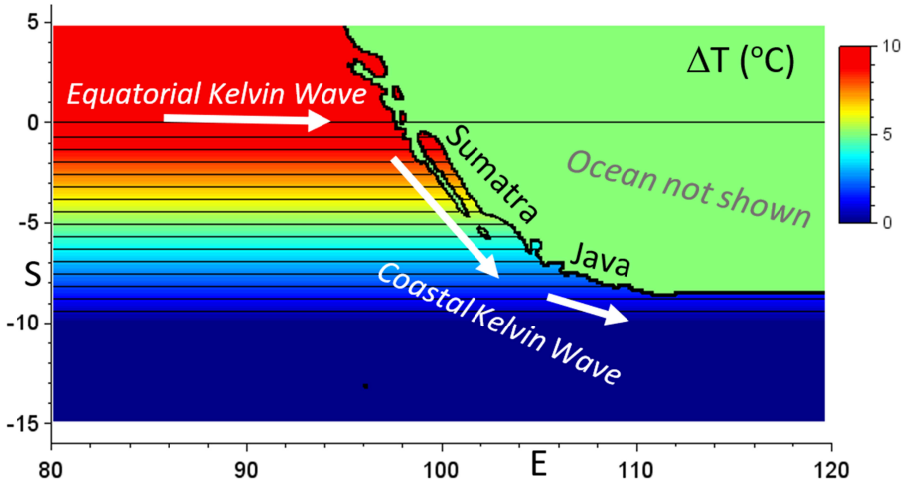

Figure 1: Model domain showing the initial distribution of an Eulerian tracer field, ΔT (^{o}C), that mimics the temperature field of the south-eastern tropical Indian Ocean. Arrows illustrate the propagation direction of equatorial and coastal Kelvin waves.

This paper uses a simple reduced-gravity model to explore the ocean's response to wind fields of two selected years that characterize the onset period (July-September) of different phases of the IOD. The underlying research question addressed is whether equatorial winds, coastal winds or both are responsible for the creation of positive IOD events.

2 Methodology

2.1 Model description

This work applies a reduced gravity-model being cast in a Cartesian coordinate system using the equatorial beta-plane approximation of the Coriolis parameter. This reduced-gravity model does not account for air-sea density fluxes or horizontal density changes. Frictional effects at the base of the surface mixed layer are also ignored. This model is governed by the equations:

$$\frac{\partial}{\partial t}\boldsymbol{u} + \boldsymbol{u}\frac{\partial}{\partial x}\boldsymbol{u} + \boldsymbol{v}\frac{\partial}{\partial y}\boldsymbol{u} - \boldsymbol{f}\boldsymbol{v} = \frac{\Delta\rho}{\rho_o}\boldsymbol{g}\frac{\partial}{\partial x}\boldsymbol{h} + \frac{\tau_x}{\rho_o} + \frac{\partial}{\partial x}\left(\boldsymbol{A_h}\frac{\partial}{\partial x}\boldsymbol{u}\right) + \frac{\partial}{\partial y}\left(\boldsymbol{A_h}\frac{\partial}{\partial y}\boldsymbol{u}\right) \quad (1)$$

$$\frac{\partial}{\partial t}\boldsymbol{v} + \boldsymbol{u}\frac{\partial}{\partial x}\boldsymbol{v} + \boldsymbol{v}\frac{\partial}{\partial y}\boldsymbol{v} + \boldsymbol{f}\boldsymbol{u} = \frac{\Delta\rho}{\rho_o}\boldsymbol{g}\frac{\partial}{\partial y}\boldsymbol{h} + \frac{\tau_y}{\rho_o} + \frac{\partial}{\partial x}\left(\boldsymbol{A_h}\frac{\partial}{\partial x}\boldsymbol{v}\right) + \frac{\partial}{\partial y}\left(\boldsymbol{A_h}\frac{\partial}{\partial y}\boldsymbol{v}\right) \quad (2)$$

$$\frac{\partial}{\partial t}\boldsymbol{h} + \frac{\partial}{\partial x}(\boldsymbol{hu}) + \frac{\partial}{\partial y}(\boldsymbol{hv}) = 0 \quad (3)$$

where (x,y) are horizontal coordinates with y = 0 marking the equator, (u,v) is horizontal

velocity, the Coriolis parameter is approximated as $f = \beta y$ with $\beta = 2.2\times10^{-11}$ $s^{-1}m^{-1}$, $\Delta\rho$ is the seawater density anomaly of the surface mixed layer, $\rho_o = 1026$ kg m^{-3} is the ambient seawater density, h is the thickness of the surface mixed layer, (τ_x, τ_y) is the wind-stress vector, and A_h is horizontal diffusivity, set to a constant value of 1000 m^2/s. Variation of A_h did not significantly alter the results. Results are expressed in terms of thermocline displacements, given by $\eta^* = h - h_o$, where $h_o = 100$ m is the initial thickness of the surface mixed layer.

Using the latest GEBCO bathymetry available on a 15 arc-second interval grid, the model equations are applied with a grid resolution of $\Delta x = \Delta y = 13{,}750$ m to the study region covering geographical longitudes from 80° to 120°E and latitudes from 15°S to 5°N (see Fig. 1), which is larger than the region (90–110°E, 10–0°S) used to calculate the DMI. For simplicity, passages of the Indonesian Throughflow including Lombok Strait and Ombai Strait are closed, and oceans on the other side of these passages are ignored in the simulations. The minimum water depth is set to 500 m, exceeding the maximum thickness of the surface mixed layer. The initial thickness of the surface mixed layer is set to 100 m throughout the model domain. The density anomaly of the surface mixed layer is set to 5 kg/m^3, which is sufficient to prevent outcropping of the thermocline during simulations. Wind stresses are calculated from wind speeds at 10-m above sea level using standard bulk formulae with a wind drag coefficient of 1.2×10^{-3}. Zero-gradient conditions are used along all open boundaries. In addition, Rayleigh-damping conditions are applied to interface displacements near the northern, southern, and eastern open boundaries. In these zones, the Rayleigh damping coefficient increases from zero to a maximum value of 0.01 over 10 grid points from a boundary.

An advection-diffusion equation is used to predict the deformation of a Eulerian tracer field, ΔT, approximating temperatures anomalies of the surface ocean. This equation is given by:

$$\frac{\partial}{\partial t}\Delta T + u\frac{\partial}{\partial x}\Delta T + v\frac{\partial}{\partial y}\Delta T = \frac{\partial}{\partial x}\left(K_h\frac{\partial}{\partial x}\Delta T\right) + \frac{\partial}{\partial y}\left(K_h\frac{\partial}{\partial y}\Delta T\right) \quad (4)$$

where K_h is also set to 1000 m^2 s^{-1}. Initially, ΔT increases linearly by 10°C from 10°S to the equator (see Figure 1), which is based on observed temperature scales. Kämpf (2009) describes the numerical treatment of (1) to (4), noting that a no-slip condition is used for the flow component parallel to a coastline.

2.2 Experimental design

The model is forced by daily CCMP v2.0 wind data averaged over the period July-September, corresponding to the development phase of IOD events (see Kämpf and Kavi, 2019). The use of daily wind data without averaging yielded similar results (not shown). The focus is placed on the contrasting seasons of two years, namely 2019 and 2009, that characterize opposite phased of the IOD. A particularly strong pIOD developed during this period in 2019 (see Lu and Ren, 2020), whereas 2009 characterizes the neutral phase of the IOD (see Kämpf and Kavi, 2019). The static, but spatially variable wind fields are linearly adjusted from zero to their final values over the first 5 simulation days to avoid the generation of unwanted dynamical disturbances. Using a numerical timestep of 120 s, the total simulation time of experiments is 60 days (2 months).

For comparison, the model simulations for both 2009 and 2019 seasons are repeated with the addition of Rayleigh-damping of interface displacements in a zone centered over the equator. The damping is of the form of:

$$\frac{\partial}{\partial t}\eta^* = -\varepsilon\eta^* \qquad (5)$$

where $\varepsilon = 0.001 \max(1-|y|/y^*,0)$ with $y^* = 200$ km. This approach allows to indirectly quantify the role that equatorial winds play in the development of pIOD events.

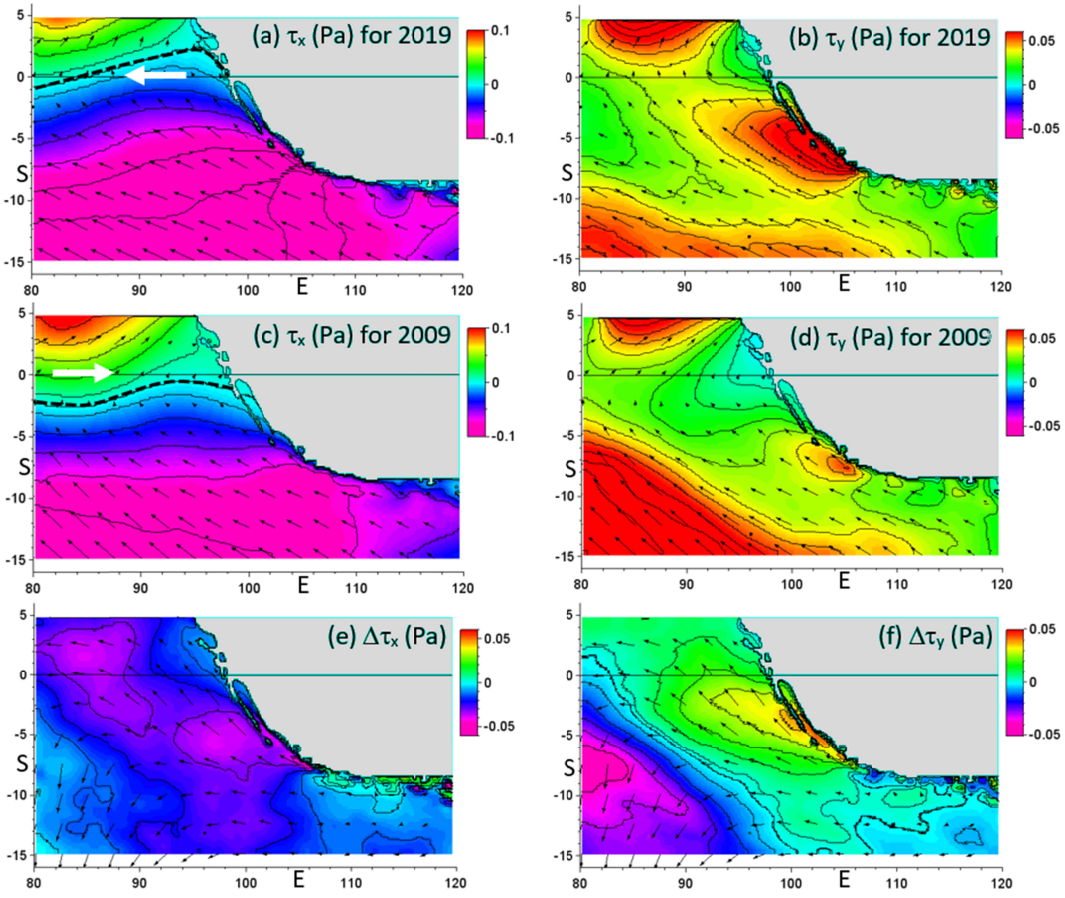

Figure 2: Horizontal distribution of the zonal and meridional components of wind stress (τ_x, τ_y) for the July-September periods of 2019, shown in panels a) and b), and 2009, shown in panels c) and d). Panels e) and f) display the anomaly maps of 2019 minus 2009 wind components. CI = 0.02 Pa in all panels. Arrows are horizontal wind vectors; only every 20th vector is displayed. Black dashed lines in panels a and b indicate the line across which the zonal wind changes direction, referred to as "turning point" in the text; arrows indicate the direction of the equatorial wind component.

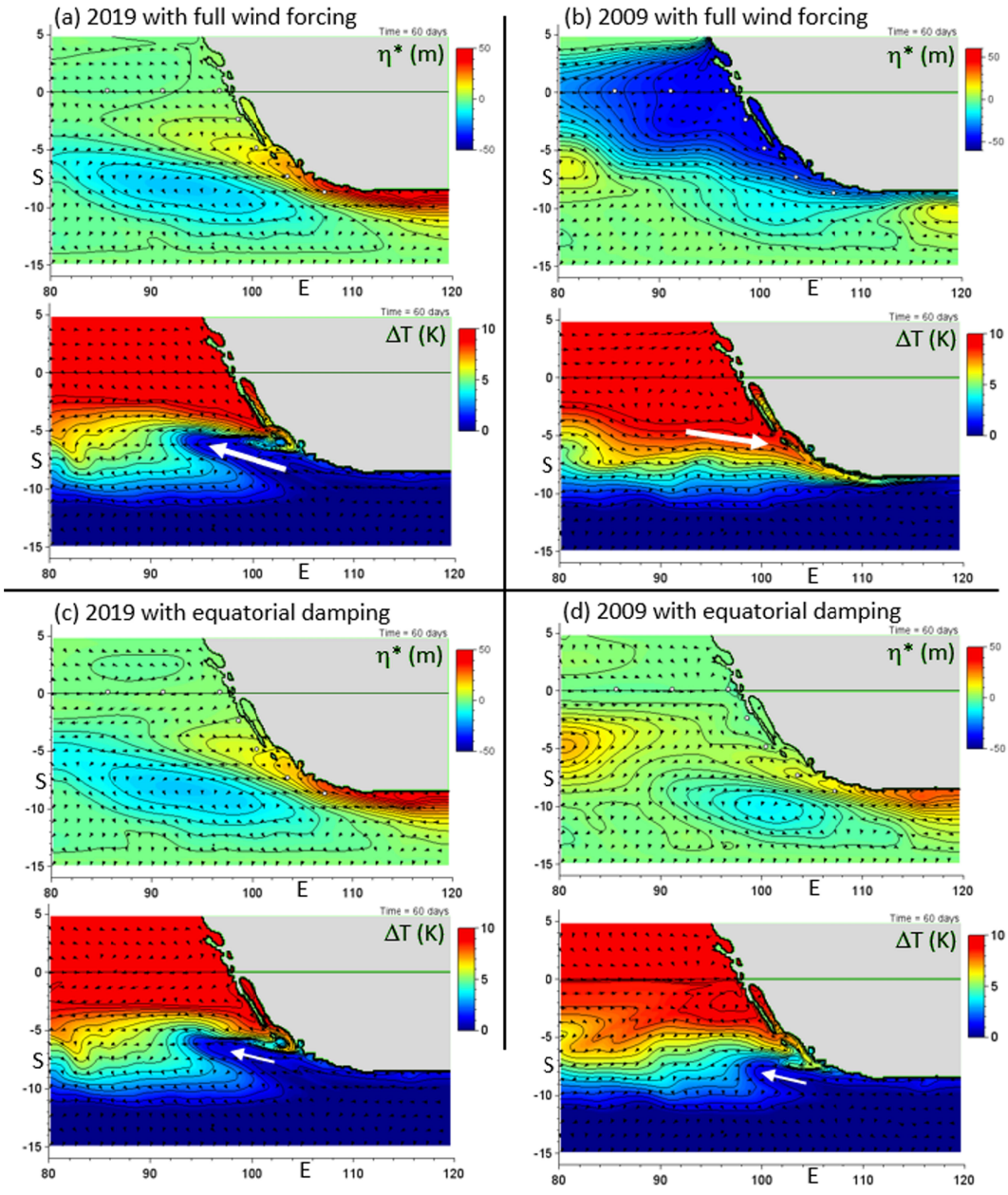

Figure 3: Horizontal distributions of interface displacement η*(m) and anomalies of the Eulerian tracer field ΔT (K) for the average wind forcing of the period July-September of the years a) 2019 and b) 2009. Panels c and d show the results for the same wind fields but with use of Rayleigh damping near the equator, which filters out equatorial wave disturbances. Small arrows represent flow velocity (every 10th vector is displayed). White arrows highlight key currents.

3 Results and discussion

There is a high similarity of the average July-September wind fields between the years of 2009 and 2019 (**Figure 2**). The general feature of the wind pattern for the period July-September is that southeasterly wind found south of the equator turns into southwesterly wind north of the

equator. However, there is a slight but important difference between the years, discussed in the following. For this purpose, we define the "turning point" as the contour line that marks the directional change of the zonal wind component U, defined by $U = 0$. In 2019, the turning point was located north of the equator in the region east from 96°E, where it established equatorial wind with an easterly component (Fig. 2a). In contrast, in 2009, the turning point was located 100-200 km south of the equator; that is, the equatorial wind had a westerly component (Fig. 2c). Hence, there is a distinct reversal of the direction of the equatorial wind component, noting that equatorial wind-stress magnitudes are generally low (0.01-0.04 Pa). The upwelling-favorable wind along Sumatra intensified in 2019, also reported by Lu and Ren (2020), which shows up as anomalies in both wind-stress components (Fig. 3e-f). Wind anomalies along Java's south coast are relatively small.

It is interesting to note that a slight northwestward displacement by ~100-200 km of the average wind field (represented by 2009 data) would largely replicate key features of the wind field characterizing the 2019 pIOD event.

The wind forcing of 2019 creates pronounced upwelling along the south coast of Java and the southwest coast of Sumatra with the vertical displacement of the thermocline exceeding 50 m after 60 days of simulation (**Figure 3a**). This upwelling is the agent to lower SSTs in waters up to ~200 km from the coast. Via the geostrophic adjustment process, the upwelling process creates dynamic pressure anomalies that lead to the formation of a northwestward flow, which is a classical upwelling jet (see Kämpf and Chapman, 2016). This flow, attaining a speed of 50 cm/s in the simulation, strongly resembles the structure of the observed South-East Sumatra Current (SESC) (Kämpf and Kavi, 2019). The advective deformation of the model's Eulerian tracer field demonstrates that the flow operates to displace colder surface water northward (Fig. 3a, lower panel). The predicted SST anomalies agree with observational evidence both in terms of magnitude and location (see Kämpf and Kavi, 2019). The zone of advective SST anomalies is located adjacent to the zone of coastal upwelling, hence effectively enlarging the zone of negative SST anomalies in the region. From this it can be concluded that advective effects play an important role in the development of pIOD events.

Note that the 2019 wind field does not induce significant thermocline variations along the equator. This implies that a downwelling effects along the equator cancel the upwelling due to the lee effect.

The slightly different wind field of 2009 produces vastly different results **(Figure 3b)**. Here the wind forcing induces downwelling in a broad zone along the equator extending along the coastlines of Sumatra and Java. Downward displacements of the thermocline are ~50 m. Geostrophic adjustment of the dynamic pressure field creates a southeastward surface flow, resembling the extension of the Equatorial Current (see Kämpf and Kavi, 2019). This surface flow operates to transport warmer, tropical water southeastward along Sumatra's coast. It is obvious that the deepening of the thermocline along Sumatra's and Java's coasts supersedes the effect of upwelling-favorable coastal winds. A downwelling coastal Kelvin wave initiated along the equator is the principal cause of this thermocline deepening.

The dominant effect of equatorial winds on IOD events becomes more apparent with the use of a Rayleigh damping zone that filters away flow divergences along the equator. Here, the

wind fields of the years 2009 and 2019 produce similar results characterized by coastal upwelling along the coasts of Java and Sumatra, and the formation of a northwestward upwelling jet (**Figure 3c-d**). There is a slight enhanced of the upwelling in 2019, which is explained by the intensification of coastal winds (see Fig. 2). These findings indirectly prove that slight changes in equatorial winds control the development of pIOD events.

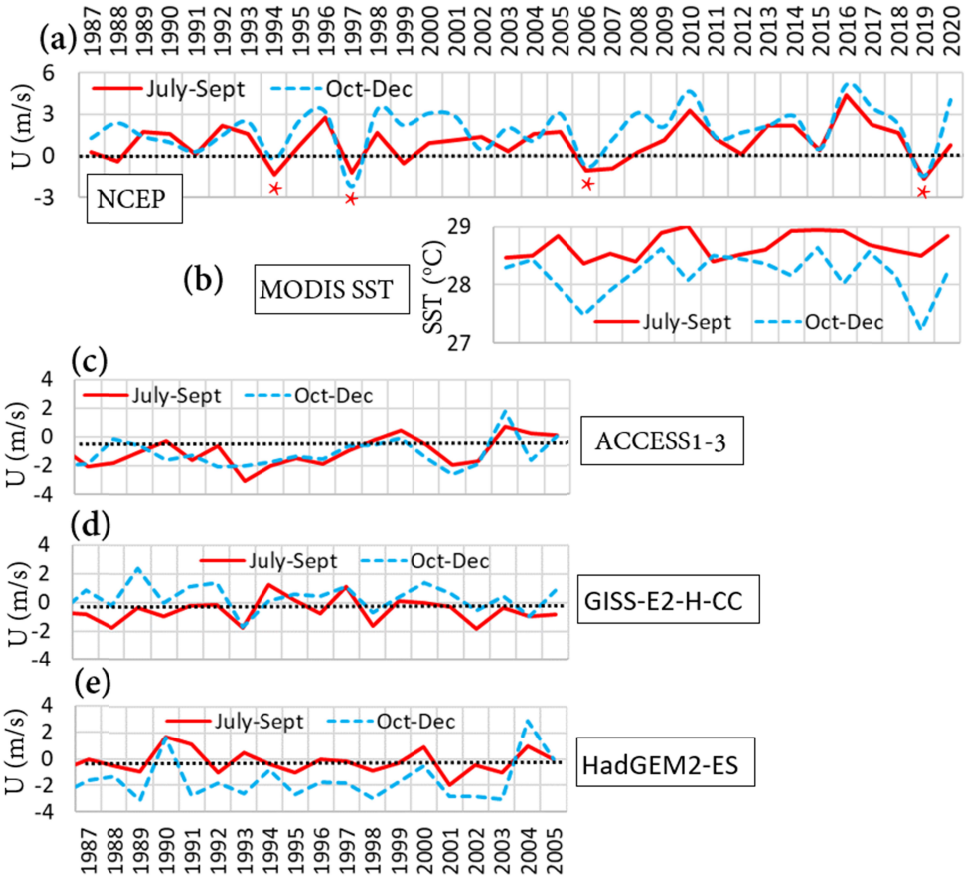

Figure 4: Time series for the periods of July-September (red full line) and October-December (blue broken line) of a) average zonal equatorial wind speed *U* (m/s) between 80°E and 100°E using NCEP reanalysis data, and b) SSTs for the region (90°E -100°E, 5°-0°) using MODIS SST data. Panels c) to e) are the same as panel a) but show selected historical CMIP5 climate model results. Red asterisks in panel a) highlight pIOD events.

Observed zonal wind speeds between 80°E and 100°E along the equator for July-September confirm that, while a westerly wind component is a typical feature for most years, pIOD events stand out by the existence of an easterly wind component (**Figure 4a**). In the pIOD seasons of 1997, 2006 and 2019, easterly wind components prevail into austral spring (October-December). The analysis by Kavi and Kämpf (2022) showed that average westerly equatorial wind components follow from subsequent westerly wind bursts associated with the formation of SETIO cyclones, noting that four cyclones formed during the IOD season of 2009, whereas only a single cyclone formed in 2019. For the period July-September, surface waters of the SETIO do not display significant SST variability within 500 km from the equator (**Figure 4b**). During this period, negative SST anomalies develop farther south (see Kämpf and Kavi, 2019). This

indicates SST anomalies near the equator are not involved in the observed variability of the equatorial zonal wind that initiates pIOD events. Consistent with this timing of events, negative SST anomalies develop delayed near the equator during October-December (see Fig. 4b).

The accurate simulation of IOD variability is a challenging issue for climate models (Luo et al., 2005; Song et al., 2008; Zhao & Hendon, 2009), which is verified here with inspection of historical model results of selected CMIP5 climate models with a focus on the zonal equatorial wind in the eastern Indian Ocean. While some models reproduced pIOD-like easterly wind conditions, such as GISS model for 1993, overall, climate model predictions of zonal equatorial winds do not agree well with observational evidence. Given the strong causal link between equatorial winds and pIOD events, demonstrated here, the predictability of IOD events by climate models is questionable.

4 Conclusions

Using a simple reduced-gravity modelling approach, this work revealed that zonal wind anomalies along the equator are pivotal in the formation or suppression of positive phases of the IOD, rather than coastal wind anomalies, previously suggested by Kämpf and Kavi (2019) and Lu and Ren (2020). Moreover, these equatorial wind anomalies develop during austral winter (July-September) in the absence of noticeable SST anomalies within 500 km from the equator. This indicates that the Bjerknes feedback is not derived involved in the initial development of pIODS events. Instead, it seems more plausible that the subtle change in equatorial wind conditions driving IOD variability is due to large-scale drivers such as the interhemispheric sea-level pressure gradient between Australia and the South China Sea/Philippine Sea, as proposed by Lu and Ren (2020). Findings of the present work has important ramifications for future climate research and the assessment of the performance of climate models.

Acknowledgments

The author does have any real or perceived financial conflicts or conflicts of interests associated with this work. This work did not receive external funding. I thank Ankit Kavi for the preparation of daily wind fields.

Open Research

All data used in this project are publicly available. CCMP V-2.0 vector wind analyses can be downloaded at http://www.remss.com/measurements/ccmp/. NCEP-NCAR reanalysis data can be downloaded at https://www.esrl.noaa.gov/psd/data/gridded/data.ncep.reanalysis.html. SST data are taken from Aqua MODIS Global Mapped 4µm Nighttime Sea Surface Temperature (SST4) Data, version R2019.0, that can be accessed at NASA's Giovanni data interface (https://giovanni.gsfc.nasa.gov/giovanni/). CMIP5 climate model data are available at http://apdrc.soest.hawaii.edu/las/v6/dataset?catitem=3588. This work used the data products of "ACCESS1-3_r1i1p1 eastward near-surface wind", "GISS-E2-H_r1i1p1 eastward near-surface wind" and "HadGEM2-ES_r1i1p1 eastward near-surface wind". The Fortran model code including forcing data will be deposited to a FAIR compliant repository at acceptance.

References

Behera, S. K., Luo, J., Masson, S., Delecluse, P., Gualdi, S., Navarra, A., & Yamagata, T. (2005). Paramount impact of the Indian Ocean dipole on the east African short rains: a CGCM study. *Journal of Climate,* 18(21), 4514–4530. doi:10.1175/jcli3541.1

Bjerknes, J. (1966). A possible response of the atmospheric Hadley circulation to equatorial anomalies of ocean temperature. *Tellus,* 18(4), 820–829. doi:10.3402/tellusa.v18i4.9712

Bjerknes, J. (1969). Atmospheric teleconnections from the equatorial Pacific. *Monthly Weather Review*, 97(3), 163–172. doi:10.1175/1520-0493(1969)097h0163:ATFTEPi2.3.CO;2

Cai, W., Cowan, T., & Sullivan, A. (2009). Recent unprecedented skewness towards positive Indian Ocean dipole occurrences and its impact on Australian rainfall. *Geophysical Research Letters,* 36(11), 1–4. doi:10.1029/2009gl037604

Cai, W., Santoso, A., Wang, G., Weller, E., Wu, L., Ashok, K., Masumoto, Y., Yamagata, T. (2014). Increased frequency of extreme Indian Ocean Dipole events due to greenhouse warming. *Nature,* 510, 254–258. doi:10.1038/nature13327

Cai, W., Wang, G., Gan, B., Wu, L., Santoso, A., Lin, X., Chen, Z., Jia, F., & Yamagata, T. (2018). Stabilised frequency of extreme positive Indian Ocean Dipole under 1.5 °C warming. *Nature Communications,* 9(1), 1419. doi:10.1038/s41467-018-03789-6

Chan, S. C., Behera, S. K., & Yamagata, T. (2008). Indian Ocean Dipole influence on south American rainfall. *Geophysical Research Letters,* 35(14), 1–5. doi:10.1029/2008gl034204

Feng, M., & Meyers, G. (2003). Interannual variability in the tropical Indian Ocean: a two-year timescale of Indian Ocean Dipole. Deep Sea Research – II. *Topical Studies in Oceanography,* 50(12–13), 2263–2284. doi:10.1016/S0967-0645(03)00056-0

Hela, I. (1976). Vertical velocity of the upwelling in the sea. *Societas Scientiarum Fennica,* 46, 9–24.

Kämpf, J. (2009). Ocean modelling for beginners: using open-source software. Berlin: Springer

Kämpf, J. (2015). Interference of wind-driven and pressure gradient-driven flows in shallow homogeneous water bodies. *Ocean Dynamics, 65,* 1399–1410. doi:10.1007/s10236-015-0882-2

Kämpf, J., & Chapman, P. (2016). Upwelling systems of the world. A scientific journey to the most productive marine ecosystems. New York: Springer International Publishing. doi:10.1007/978-3-319-42524-5

Kämpf, J., & Kavi, A. (2019). SST variability in the eastern intertropical Indian Ocean – On the search for trigger mechanisms of IOD events. *Deep Sea Research – II. Topical Studies in Oceanography,* 166, 64–74. doi:10.1016/j.dsr2.2018.11.010

Kavi, A., & Kämpf, J. (2022). Synoptic-scale atmospheric cyclones in the South-East Tropical Indian Ocean (SETIO) and their relation to IOD variability. *Journal of Southern Hemisphere Earth Systems Science,* 72, 191–201. doi:10.1071/ES22020

Li, T., Wang, B., Chang, C. P., & Zhang, Y. S. (2003). A theory for the Indian Ocean dipole–zonal mode. *Journal of the Atmospheric Sciences*, 60(17), 2119–2135. doi:10.1175/1520-0469(2003)060<2119:ATFTIO>2.0.CO;2

Moihamette, F., Pokam, W. M., Diallo, I., & Washington, R. (2022). Extreme Indian Ocean dipole and rainfall variability over Central Africa. International Journal of Climatology, 42(10), 5255– 5272. doi:.10.1002/joc.7531

McPhaden, M. J. (1999). Genesis and evolution of the 1997–98 El Niño. *Science*, 283, 950–954. doi:10.1126/science.283.5404.950

Qiu, Y., Cai, W., Guo, X., & Ng, B. (2014). The asymmetric influence of the positive and negative IOD events on China's rainfall. Scientific Reports, 4(1), 1–6. doi:10.1038/srep04943

Saji, N. H., Goswami, B. N., Vinayachandran, P. N., & Yamagata, T. (1999). A dipole mode in the tropical Indian Ocean. *Nature,* 401(6751), 360–363. doi:10.1038/43854

Saji, N. H., & Yamagata, T. (2003). Possible impacts of Indian Ocean dipole mode events on global climate. *Climate Research,* 25, 151–169. doi:10.3354/cr025151

Webster, P. J., Moore, A. M., Loschnigg, J. P., & Leben, R. (1999). Coupled ocean-atmosphere dynamics in the Indian Ocean during 1997–98. *Nature,* 401, 356–359. doi.org/10.1038/43848